

3.6–7.9 μm Photometry of L and T Dwarfs and the Prevalence of Vertical Mixing in their Atmospheres

S. K. Leggett

Gemini Observatory, 670 N. A'ohoku Place Hilo HI 96720

sleggett@gemini.edu

D. Saumon

Los Alamos National Laboratory, MS P365, Los Alamos, NM 87545

M. S. Marley

MS 245-3, NASA Ames Research Center, Moffett Field, CA 94035

T. R. Geballe

Gemini Observatory, 670 N. A'ohoku Place, Hilo HI 96720

D. A. Golimowski and D. Stephens

Department of Physics & Astronomy, Johns Hopkins University, 3400 North Charles Street, Baltimore, MD 21218

and

X. Fan

Steward Observatory, 933 N. Cherry Avenue, Tucson, AZ 85721

ABSTRACT

We present new L' (3.75 μm) photometry of six L and T dwarfs, and M' (4.70 μm) photometry of ten L and T dwarfs, observed at Gemini (North) Observatory, and new 3.55, 4.49, 5.73 and 7.87 μm photometry of nine L and T dwarfs, obtained with the *Spitzer Space Telescope*. The sample includes unusually blue and red dwarfs selected from our near-infrared studies. The data are combined with previously published L' , M' and *Spitzer* photometry of L and T dwarfs, and trends of colors with spectral type and other colors are examined. Recent model atmospheres by Marley and Saumon are used to generate synthetic colors for ranges of effective temperature, gravity, grain sedimentation efficiency, metallicity and vertical mixing efficiency. We explore how these parameters affect the mid-infrared colors of L and T dwarfs and find that the data are modelled satisfactorily only if substantial vertical mixing occurs in both L- and T-dwarf atmospheres. The location and range of the L and T dwarf sequences in IRAC color-color and color-magnitude diagrams is also only reproduced if this mixing occurs, with a range of efficiency described by $K_{zz} \sim 10^2\text{--}10^6 \text{ cm}^2 \text{ s}^{-1}$. The colors of the unusually red dwarfs are best reproduced by non-equilibrium models with low sedimentation efficiency, i.e. thick cloud decks, and the colors of the unusually blue dwarfs by non-equilibrium models with high sedimentation efficiency, i.e. thin cloud decks. The $K\text{--}L'$ and *Spitzer* [3.55]–[4.49] colors can be used as indicators of effective temperature for L and T dwarfs, but care must be taken to include gravity and metallicity effects for late-T dwarfs and vertical mixing for both late-L and T dwarfs.

Subject headings: infrared: stars — stars: low-mass, brown dwarfs

1. Introduction

The Sloan Digital Sky Survey (SDSS; York et al. 2000) and the Two Micron All Sky Survey (2MASS; Beichman et al. 1998, Skrutskie et al. 2006) have revealed large numbers of ultracool low-mass field dwarfs, known as L and T dwarfs. The effective temperatures (T_{eff}) of L dwarfs are $\sim 1450\text{--}2200$ K, and those of currently known T dwarfs are $\sim 700\text{--}1450$ K (Golimowski et al. 2004a, hereafter G04; Vrba et al. 2004).

As T_{eff} drops below that of the late-M dwarfs, the spectral energy distributions (SEDs) of ultracool dwarfs are dramatically changed by chemical and cloud processes in their atmospheres. First, iron and silicate grains condense high in the atmosphere and form clouds that veil gaseous absorption bands and redden the near-infrared colors of L dwarfs. As T_{eff} falls, these clouds form progressively deeper in the atmosphere and become more optically thick. By $\sim 1500\text{--}1700$ K, the effect of the clouds on the emergent flux is greatest (Ackerman & Marley 2001). At lower T_{eff} , the clouds lie near or below the base of the wavelength-dependent photosphere and only marginally affect the flux distributions of T dwarfs. The rapidity, with respect to T_{eff} , with which the clouds diminish is not well understood and several mechanisms have been proposed (e.g. Burgasser et al. 2002b, Burrows, Sudarsky & Hubeny 2006, Knapp et al. 2004, hereafter K04). G04 showed that T_{eff} is nearly constant ($\sim 1300\text{--}1500$ K) for spectral types L7 to T4. Thus, for these spectral types, the primary cause of the observed spectral change is apparently rapid alteration of the vertical properties and distribution of the cloud, over a small range in T_{eff} . The changing cloud properties alter the optical depths and brightness temperatures from which the flux emerges. As the clouds depart, the upper atmosphere cools and CH_4 supplants CO as the dominant carbon-bearing molecule. CH_4 appears in the $3\text{--}4\text{ }\mu\text{m}$ spectra of mid-L dwarfs (Noll et al. 2000), the $2.2\text{--}2.5$ and $8\text{ }\mu\text{m}$ spectra of late-L dwarfs (Geballe et al. 2002; Roellig et al. 2004; Cushing et al. 2006), and the $1.6\text{ }\mu\text{m}$ spectra of T0 dwarfs (Geballe et al. 2002). Together, increasing CH_4 absorption and sinking cloud decks cause progressively bluer near-infrared colors of T dwarfs.

Over 500 ultracool field dwarfs have been con-

firmed and studied in the near-infrared (e.g. Burgasser et al. 2006b, Chiu et al. 2006 (hereafter C06), Kendall et al. 2004, Tinney et al. 2005). Our group has so far obtained accurate J , H , and K photometry on the Mauna Kea Observatories (MKO) system (Simons & Tokunaga 2002, Tokunaga et al. 2002) and $R \approx 500$, $0.9\text{--}2.5\text{ }\mu\text{m}$ spectroscopy for 102 L dwarfs and 65 T dwarfs. This sample is summarized by K04 and C06. Leggett et al. (2002) and G04 extended our study to longer wavelengths, presenting L' ($3.75\text{ }\mu\text{m}$) and M' ($4.70\text{ }\mu\text{m}$) photometry for a subset of the JHK sample. In this paper, we extend our study further by presenting broadband photometry for wavelengths up to $7.9\text{ }\mu\text{m}$.

The $3\text{--}15\text{ }\mu\text{m}$ mid-infrared region is interesting for ultracool-dwarf studies for many reasons. This region contains molecular absorption bands of CH_4 , CO, H_2O and NH_3 (Cushing et al. 2006) that are prominent in the spectra of ultracool dwarfs at various temperatures. Figure 1 shows observed and synthetic $3\text{--}10\text{ }\mu\text{m}$ spectra for late-L and T dwarfs and identifies the principal absorbing species. The vibrotational line lists for CH_4 , NH_3 and H_2O are more complete in the mid-infrared than the near-infrared, so the uncertainties in the synthetic mid-infrared spectra are smaller than those in the near-infrared spectra. Also, the mid-infrared flux emerges from photospheric regions that have a much smaller range of brightness temperatures than those giving rise to the near-infrared flux (Ackerman & Marley 2001). Hence the mid-infrared spectrum should be easier to interpret than the near-infrared spectrum. Furthermore, mid-infrared photometry is more sensitive than near-infrared photometry to vertical mixing of trace species, which can result in photospheric chemical abundances very different from equilibrium (Saumon et al. 2003; G04).

Obtaining mid-infrared photometry and spectroscopy with ground-based telescopes is difficult, due to the high and rapidly varying background at these wavelengths, and to the strong telluric absorption bands of CH_4 , CO, CO_2 , H_2O , N_2O and O_3 . The *Spitzer Space Telescope* (Werner et al. 2003) has made possible observations at these and longer wavelengths that were previously impossible from the ground. We are using *Spitzer's* Infrared Array Camera (IRAC; Fazio et al. 2004) and Infrared Spectrograph (IRS; Houck et al. 2004)

to obtain 3.6–7.9 μm photometry and 6–15 μm low-resolution spectra of late-L and T dwarfs. In this paper, we present the IRAC results along with ground-based L' and M' photometry obtained using the Near InfraRed Imager and spectrograph (NIRI; Hodapp et al. 2003) at the Gemini (North) Observatory. The IRS spectra will be presented in a future paper.

2. Observations

2.1. Gemini NIRI L' and M' Photometry

We obtained MKO L' and/or M' images of 12 late-L and T dwarfs, listed in Table 1, on 10 dry and photometric nights between UT 2004 April 05 and UT 2005 January 28. The data were obtained in queue-observing mode through programs GN-2004A-Q-16 and GN-2004B-Q-43, using Gemini Observatory’s NIRI. The half-power bandpasses for the MKO L' and M' filters (Simons & Tokunaga 2002, Tokunaga et al. 2002) are shown in Figure 1 and listed in Table 2. Because the sky is bright at these wavelengths, we used NIRI’s smallest pixel scale ($0''.022 \text{ pix}^{-1}$) to avoid saturating the detector. The full array readout was used, providing a field of view of $22''.5 \times 22''.5$. Given the small field of view, we acquired each target using proper-motion-corrected coordinates (if available) and a short J -band verification image. During the L' and M' exposures, the target was sequentially offset from the center of the detector toward each of the four corners, generating a four-position dither pattern with $6''$ offsets. Offset guide stars were used. Each L' image comprised 24 coadded exposures of 0.8 s, and each M' image comprised 34 coadded exposures of 0.5 s. The total observation time per target was typically 1.5 hr, most of which was spent on the M' exposures. Each set of science images was accompanied by contemporaneous dark frames and images of bright photometric standard stars (Leggett et al. 2003) taken with the same filters. Flat fields were generated by median-stacking the dithered science images.

The data were reduced using a version of the astronomical imaging pipeline ORAC-DR (Cavanagh et al. 2003) modified for NIRI.¹ The

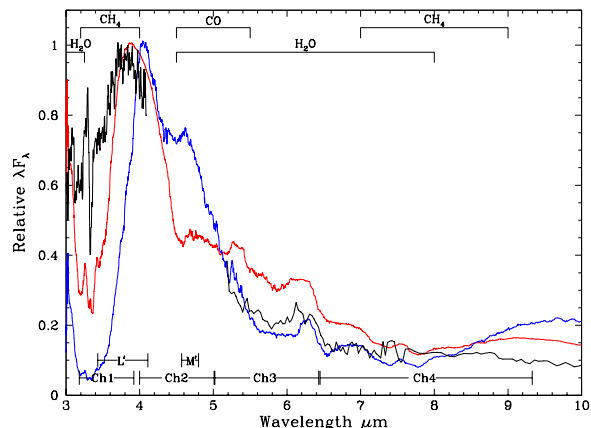


Fig. 1.— Observed and synthetic spectra of late-L and T dwarfs (normalized to peak flux) in the wavelength interval where we report new photometry. The black curves are NIRI and IRS spectra of the L9 dwarf 2MASS J09083803+5032088 (Stephens private communication). The red curve is a synthetic spectrum for $T_{\text{eff}} = 1400 \text{ K}$, $f_{\text{sed}} = 2$, and $\log g = 5$, representing late-L types, and the blue curve is a synthetic spectrum for $T_{\text{eff}} = 1000$, $f_{\text{sed}} = 4$, and $\log g = 5$, representing mid-T types (Marley & Saumon, private communication). Strong molecular absorption bands are indicated, as are the bandpasses of the MKO L' , MKO M' and IRAC channels 1–4 filters: [3.55], [4.49], [5.73], [7.87].

¹The ORAC-DR Imaging Data Re-
duction User Guide is available at
<http://www.starlink.ac.uk/star/docs/sun232.htx/sun232.html>.

pipeline uses Starlink routines to perform bad-pixel masking, dark subtraction, differencing of adjacent pairs, flat-field creation and division, feature detection and matching between object frames, and resampling. The final combined image, termed a mosaic, is generated with intensity offsets applied to give the most consistent results in the overlapping regions of the dithered images. Pairwise differencing allows more accurate sky subtraction and flat-fielding, although it yields positive and negative images of each source in the mosaics. The mosaics were binned 3×3 to enhance the visibility of the L and T dwarfs. The final pixel scale was therefore $0''.066 \text{ pix}^{-1}$.

We performed aperture photometry on both the positive and negative images of the L and T dwarfs using apertures of diameter $1''$ – $2''$. We defined the uncertainty to be the difference between the measurements of the positive and negative images. This difference is similar to, or slightly larger than, the formal error calculated from the noise. Table 1 lists the resulting L' and M' magnitudes, as well as any previously published measurements. Henceforth, we use the weighted averages of the new and previously published measurements of all the dwarfs except 2MASS J15031961+2525196, whose previous uncertain M' measurement is discarded in favor of the NIRI value.

2.2. *Spitzer* Four-Channel Photometry

We obtained IRAC four-channel photometry (3.55 , 4.49 , 5.73 , and $7.87 \mu\text{m}$) of the nine L and T dwarfs listed in Table 3 between UT 2005 July 23 and UT 2006 July 06. The data were obtained as part of our Cycle 2 *Spitzer* General Observer program # 20514. The half-power bandpasses for the four channels are listed in Table 2 and indicated in Figure 1. All four channels have 256×256 -pixel detectors with a pixel size of $1''.2 \times 1''.2$, yielding a $5'.2 \times 5'.2$ field of view. Two adjacent fields are imaged in pairs (channels 1 and 3; channels 2 and 4) using dichroic beam splitters. The telescope is then nodded to image a target in all four channels.² We used exposure times of 30 s and a 5-position medium-sized (52 pixels) dither pattern repeated one to four times. The total observing time per target ranged from 11 to 26 minutes. The full ar-

ray was read out.

The data were reduced using the post-basic-calibration data mosaics generated by version 14 of the IRAC pipeline.³ The mosaics were flat-fielded and flux-calibrated using super-flats and global primary and secondary standards observed by *Spitzer*. We performed aperture photometry on the L and T dwarfs using apertures of radii 3–7 pixels. The dwarfs were usually isolated and well detected, so apertures of 7 pixels could be used. We applied channel-dependent aperture corrections as described in Chapter 5 of the IRAC Data Handbook.³ For channels 1 to 3, the correction for the 7-pixel aperture is 3%, for the 5-pixel aperture it is 5–6% and for the 3-pixel aperture it is 11–12%. For channel 4, these corrections are 4%, 7%, and 22%. We derived photometric errors from the uncertainty images that are provided with the post-basic-calibration data. The photometry was converted from milliJanskys to magnitudes on the Vega system using the zero-magnitude fluxes given in the IRAC Data Handbook (280.9 , 179.7 , 115.0 , and 64.1 Jy for channels 1 to 4, respectively). The fluxes, magnitudes, and errors for the observed dwarfs are given in Table 3. Note that in addition to the errors in Table 3, there are absolute calibration uncertainties of 2–3%. There are also similarly-sized systematic uncertainties introduced by pipeline dependencies, as we found by comparing the photometry produced by pipeline versions 12, 13 and 14 for seven of our targets. Photometry produced by versions 12 and 14 agreed well, to typically 4%, however version 13 produced fainter magnitudes than the other two pipelines, by $\sim 7\%$. The *Spitzer* helpdesk team recommend version 14 of the pipeline, and suggest that version 13 used an over-aggressive pixel rejection algorithm. We adopt the total photometric uncertainty to be the sum in quadrature of the values given in Table 3 plus 3%.

IRAC flux densities follow the convention established by the *Infrared Astronomical Satellite* (*IRAS*) and other missions. The IRAC flux density at a nominal wavelength assumes that the source has a spectrum described by $F_\nu \propto \nu^{-1}$. However, this assumption is not valid for the SEDs of late-L and T dwarfs (Figure 1); $\lambda \times F_\lambda$ is not

²See Fazio et al. (2004) and the IRAC Users Manual at <http://ssc.spitzer.caltech.edu/irac/descrip.html>

³Further information can be found at <http://ssc.spitzer.caltech.edu/irac/dh/>

constant in these cases. Hence the fluxes given in Table 3 are not representative of the nominal wavelengths given in Table 2. For example, the $3.55\ \mu\text{m}$ and $7.87\ \mu\text{m}$ IRAC fluxes of the L9 dwarf shown in Figure 1 differ by $\sim 30\%$ and $\sim 10\%$, respectively, from the actual fluxes at those wavelengths measured by *Spitzer's* IRS. If the source spectrum is known, the quoted IRAC flux for a nominal wavelength λ_0 can be expressed as

$$f_{\nu}^{IRAC}(\lambda_0) = \int (\nu_0/\nu) f(\nu) S(\nu) d\nu \bigg/ \int (\nu_0/\nu)^2 S(\nu) d\nu$$

where $f(\nu)$ is the source spectrum and $S(\nu)$ is the system response function (Cushing et al. 2006).

To put our data into context, we augment our sample with the IRAC photometry of M, L, and T dwarfs from Patten et al. (2006, hereafter P06), and include the photometry of two T dwarfs discovered in IRAC images by Luhman et al. (2006).

3. Colors and Spectral Types

Figure 2 shows the differences between IRAC channel 1 ($3.55\ \mu\text{m}$) and MKO L' ($3.75\ \mu\text{m}$) magnitudes and between IRAC channel 2 ($4.49\ \mu\text{m}$) and MKO M' ($4.70\ \mu\text{m}$) magnitudes, as functions of spectral type. The data are from this work, Leggett et al. (2002), Reid & Cruz (2002), G04, and P06. IRAC channels 1 and 2 span wavelengths similar to those of L' and M' , respectively (Figure 1), and correlations can be used to check the consistency of *Spitzer* and ground-based data.

Figure 2 shows that the IRAC channel 1 magnitudes (denoted [3.55]) become fainter than L' magnitudes for later spectral types. This behavior is expected because channel 1 samples more of the strong center of the $3.3\ \mu\text{m}$ CH_4 absorption band, and less of its long-wavelength wing and flux peak near $4\ \mu\text{m}$, compared to the L' bandpass (see Figure 1). The T7.5 dwarf 2MASS J12171110-0311131 is clearly anomalous in this plot; we discuss it further in §4. The difference between IRAC channel 2 ([4.49]) and M' is fairly constant ([4.49]– $M' \approx -0.3$) for all types, with the exception of the extremely red late-L dwarf 2MASS J22443167+2043433 (§4). Both channel 2 and M' sample H_2O and CO bands, even among T dwarfs (§4). Although channel 2 is much wider than M' , the filters are similarly sensitive to changes with spectral type.

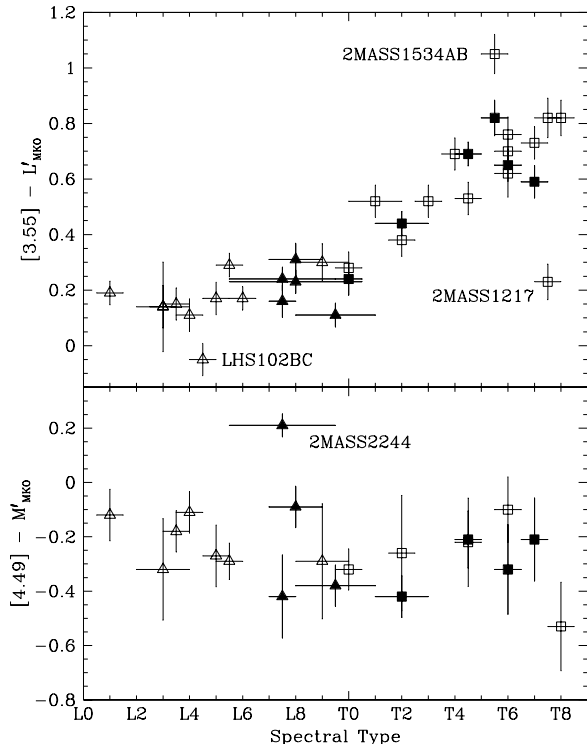


Fig. 2.— Comparison of MKO L' ($3.75\ \mu\text{m}$) and M' ($4.70\ \mu\text{m}$) magnitudes with the IRAC channel 1 ([3.55]) and channel 2 ([4.49]) magnitudes. Triangles represent L dwarfs and squares represent T dwarfs. Filled symbols are data presented in this work; open symbols are data from Leggett et al. (2002), Reid & Cruz (2002), G04, and P06. The following dwarfs are identified with abbreviated names: 2MASS J12171110-0311131, 2MASS J1534498-295227AB and 2MASS J2244316+204343.

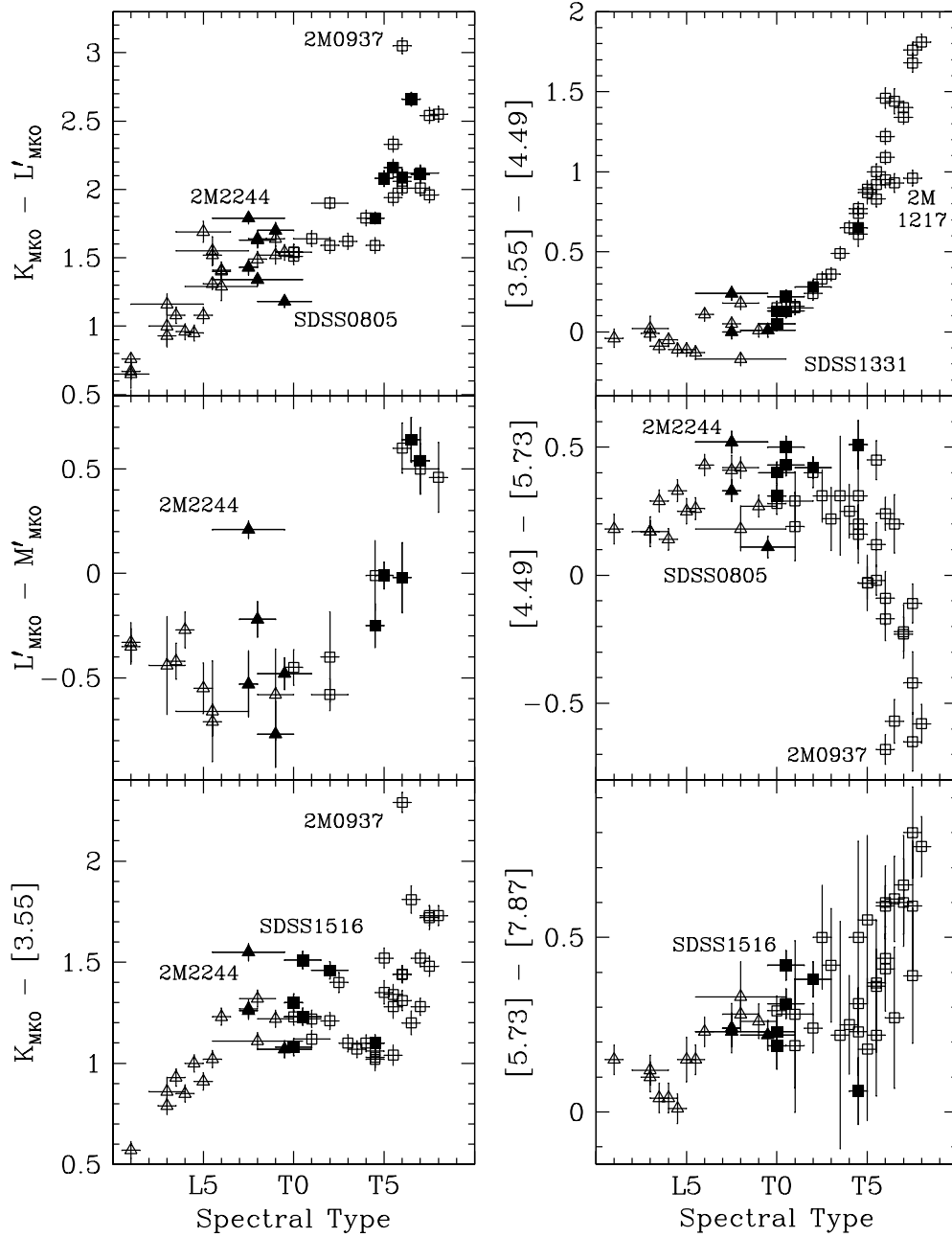


Fig. 3.— Colors as a function of spectral type. The symbols are described in Figure 2. Here, and in the following figures, open symbols are data from Leggett et al. (2002), Reid & Cruz (2002), G04, P06 and Luhman et al. (2006). The following unusually blue or red dwarfs are identified and discussed in the text: 2MASS J0937347+293142, 2MASS J12171110-0311131, 2MASS J2244316+204343, SDSS J080531.80+481233, SDSS J133148.90-011651.4, SDSS J151643.01+305344.4.

Figure 3 shows various IRAC and MKO $KL'M'$ colors plotted as functions of spectral type. The data are taken from this work, Leggett et al. (2002), Reid & Cruz (2002), K04, G04, C06, Luhman et al. (2006) and P06. All of the colors show scatter at the ~ 0.5 mag level from mid-L to early-T types, but general trends and some peculiarities can be seen. 2MASS J22443167+2043433, the reddest L dwarf currently known (Dahn et al. 2002; K04), is clearly anomalous in many colors. SDSS J080531.80+481233.0 and SDSS J133148.90-011651.4, both unusually blue in the near-infrared (K04), are also anomalously blue in the IRAC [4.49]–[5.73] and [3.55]–[4.49] colors. SDSS J151643.01+305344.4, a red early-T dwarf (C06), is also red in K –[3.55] and [5.73]–[7.87]. Thus, the unusual traits seen in these dwarfs at shorter wavelengths often persist at longer wavelengths. 2MASS J09373487+2931409, which is extremely red in K – L' and K –[3.55], has suppressed K -band flux most likely due to very strong H_2 absorption (Burgasser et al. 2002a).

4. Interpretation of Colors and Luminosities

In this section, we compare the observed IRAC and MKO colors with the predicted colors from model atmospheres, and investigate the physical parameters that can produce the observed trends and variations seen in Figure 3.

4.1. Description of Model Atmospheres

State-of-the-art models of ultracool-dwarf atmospheres have been developed by members of our team (Ackerman & Marley 2001; Marley et al. 2002; Saumon et al. 2003; and will be further described in an upcoming paper). These models yield temperature-pressure-composition structures under conditions of radiative-convective equilibrium using the thermal radiative transfer source function technique of Toon et al. (1989). The gas opacity database includes the molecular lines of H_2O , CH_4 , CO , NH_3 , H_2S , PH_3 , TiO , VO , CrH , FeH , CO_2 , HCN , C_2H_2 , C_2H_4 , and C_2H_6 , the atomic lines of the alkali metals (Li, Na, K, Rb and Cs), and continuum opacity from H_2 collisionally induced absorption (CIA), H_2 , H and He Rayleigh scattering, bound-free opacity from H and H_2^+ , and free-free opacity from He, H_2^- , and

H_2^+ . The models also allow opacity from arbitrary Mie-scattering particles.

The radiative transfer code is closely coupled to cloud models that use a sedimentation efficiency parameter, f_{sed} , to describe the balance between the downward sedimentation of condensates and the upward convection that replenishes the grains. Large values of f_{sed} correspond to rapid growth of large grains, which then quickly fall out of the atmosphere and yield physically and optically thin clouds. When f_{sed} is small, the grains grow more slowly and the clouds are thicker. The models have been successfully applied to the atmospheres of brown dwarfs and Jupiter (Ackerman & Marley 2001; K04; G04).

The models have been further advanced to include vertical mixing, which draws up chemical species from the well-mixed, deep, hot layers into the cool radiative photosphere. Although the photosphere would be expected to be stable and in chemical equilibrium, even a small degree of mixing (such as is commonly observed in the stratospheres of the solar system’s giant planets) enhances the abundances of stable species like CO and N_2 relative to their chemical equilibrium values, while those of H_2O , CH_4 and NH_3 are reduced (Fegley & Lodders 1996, Lodders & Fegley 2002, Saumon et al. 2003, 2006). This phenomenon has been observed in planetary atmospheres (Noll et al. 1988, Noll & Larson 1991, Fegley & Lodders 1994, Bézard et al. 2002) and in brown dwarfs (Noll et al. 1997, Griffith & Yelle 1999, Saumon et al. 2000, 2006). In the convection zone that forms in the lower atmosphere, mixing is vigorous and occurs on a time scale $\tau_{mix} = H_p/v_{conv}$ where H_p is the pressure scale height and v_{conv} is the convective velocity, obtained from the mixing length theory. The physical process of mixing in the radiative zone is not known but it should take place on a much longer time scale. For lack of a theory of mixing in brown dwarf atmospheres, it is assumed to be a diffusive process and the mixing time scale is given by $\tau_{mix} = H_p^2/K_{zz}$, where K_{zz} is the coefficient of eddy diffusivity, considered a free parameter here. For the present study, models have been calculated with $K_{zz} = 0$ (no mixing, chemical equilibrium), 10^2 and 10^4 $cm^2 s^{-1}$ in the radiative zone. For comparison, the mixing time scale in the convection zone would correspond to values of $K_{zz} \approx 10^7$ – 10^9 $cm^2 s^{-1}$.

We have generated a large grid of models with ranges of T_{eff} , surface gravity g , f_{sed} , metallicity $[M/H]$, and mixing coefficient K_{zz} . In this paper we treat the dynamical parameters, K_{zz} and f_{sed} , as independent variables, in the same way as we treat g and T_{eff} . However, the global properties of each dwarf must ultimately define the true properties of the cloud, and the vigor of atmospheric mixing. Two otherwise identical L dwarfs, for example, could not exhibit two different sedimentation efficiencies and eddy diffusion coefficients. Eventually we will be able to treat K_{zz} and f_{sed} as functions of other physical properties, but this cannot happen until we understand how differences in metallicity, rotation rate, effective temperature, and gravity impact sedimentation and mixing in the atmosphere. Thus for the time being we treat K_{zz} and f_{sed} as independent variables, and use them to understand the ranges of behaviour manifested by the known objects.

Saumon et al. (2006) have validated the models by reproducing the entire red through mid-infrared spectrum of the T7.5 dwarf Gl 570D. Cushing et al. (in preparation) also find very good agreement between the model spectra and the observed $zJHKL'$ and IRS spectra of L0–T4 dwarfs. Work in progress comparing the calculated and observed near-infrared colors of L and T dwarfs shows that L dwarfs are well represented by models with $f_{\text{sed}} = 1$ –2, while T dwarf colors are well matched by models with $f_{\text{sed}} = 4$ or by cloudless models (i.e., the clouds lie below the photosphere at all wavelengths). Finally we note that because the models are complex and CPU-intensive, not all combinations of all parameters are available at this time.

4.2. Comparison of Models and Data

Figures 4, 5, and 6 each show four color–color diagrams that compare new and previously published 2.2–7.9 μm photometry with synthetic colors generated from models covering appropriate ranges of T_{eff} , f_{sed} , $\log g$, and K_{zz} . Generally, the model sequences are generated for $500 \leq T_{\text{eff}} \leq 2400$ K in steps of 100 K. However, the dustiest ($f_{\text{sed}} = 1$ and 2) models with vertical mixing ($K_{zz} = 10^2$ and $10^4 \text{ cm}^2 \text{ s}^{-1}$) are generated for the smaller range $800 \leq T_{\text{eff}} \leq 2400$ K because calculating cold, dusty, atmospheres with mixing is difficult and CPU intensive. This limitation does

not affect our analysis or conclusions because the condensate cloud decks are expected to lie below the photosphere for $T_{\text{eff}} \lesssim 1000$ K. Consequently, we do not consider inappropriate dusty models for mid- to late-T dwarfs or cloudless models for early- to mid-L dwarfs. All model sequences assume solar metallicity, except for one metal-poor cloudless sequence.

Figure 4 demonstrates the colors’ sensitivity to gravity for the two extremes of cloud properties: a model with $f_{\text{sed}} = 1$ and a completely cloudless model. Both models assume no vertical mixing. The gravities shown ($\log g = 4.5, 5.0$ and 5.5) correspond to ~ 15 –75 Jupiter masses for ages greater than 0.3 Gyr (Burrows et al. 1997), which are appropriate for our field sample with $700 \lesssim T_{\text{eff}} \lesssim 2200$ K. Figure 5 shows sequences for $\log g = 5.0$ and a full range of sedimentation parameters, $f_{\text{sed}} = 1, 2, 3, 4$, and cloudless, without vertical mixing. It also shows a metal-poor ($[M/H] = -0.3$), $\log g = 5.0$, cloudless sequence. Figure 6 shows $f_{\text{sed}} = 1, 2, 3$, and cloudless sequences for $\log g = 5.0$, with vertical mixing parameters of $K_{zz} = 10^2$ and $10^4 \text{ cm}^2 \text{ s}^{-1}$.

In general, the varying colors of brown-dwarf model spectra are not straightforward functions of T_{eff} , gravity, composition, and f_{sed} . One must also consider the variations in chemistry and overall gas and cloud opacity that affect the depth of the “photosphere.” The relative strengths of absorption bands in the spectrum are complex functions of all these parameters. For the sake of brevity and clarity, we will explain the trends for those cases where the interpretation is clear.

4.2.1. Gravity

Figure 4 indicates that gravity only impacts significantly (at the $\gtrsim 20\%$ level) the K – L' , K – $[3.55]$, and $[4.49]$ – $[5.73]$ colors of mid- to late-T dwarfs. The $[5.73]$ – $[7.87]$ color is not significantly impacted, nor are any of the colors of dusty or cloudless dwarfs earlier than type T6 (although the absolute magnitudes can differ, as we discuss in §5).

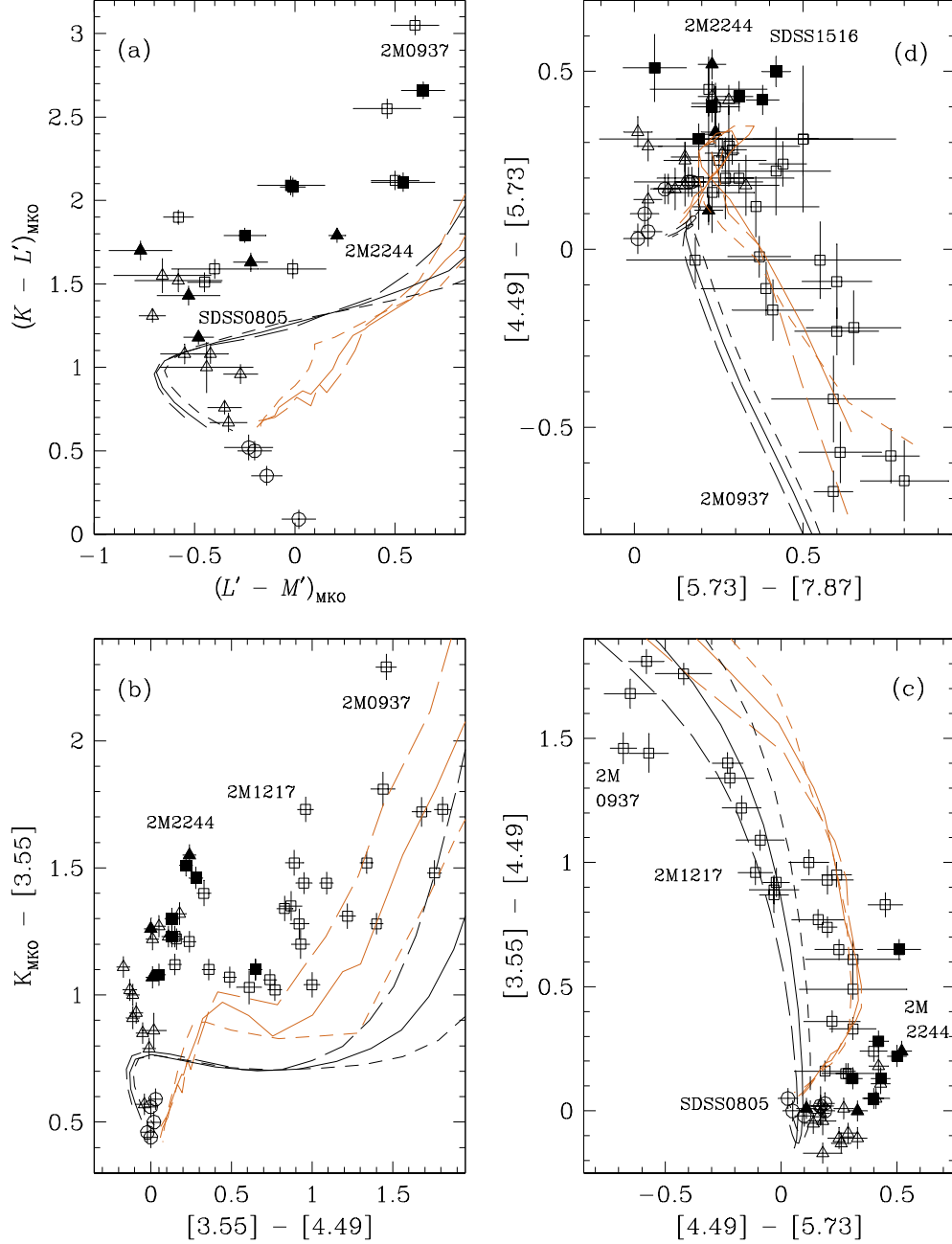


Fig. 4.— Color-color diagrams and the effect of gravity: (a) $K-L'$ vs. $L'-M'$, (b) $K-[3.55]$ vs. $[3.55]-[4.49]$, (c) $[3.55]-[4.49]$ vs. $[4.49]-[5.73]$, and (d) $[4.49]-[5.73]$ vs. $[5.73]-[7.87]$. Circles represent M dwarfs, triangles represent L dwarfs, and squares represent T dwarfs. These dwarfs are identified: 2MASS J0937347+293142, 2MASS J12171110-0311131, 2MASS J2244316+204343, SDSS J080531.80+481233 and SDSS J151643.01+305344.4. The curves show the synthetic colors as a function of T_{eff} for two cloud models ($f_{\text{sed}} = 1$ - orange curves; cloudless - black curves), three gravities ($\log g = 4.5$ - short-dashed curves; $\log g = 5.0$ - solid curves; $\log g = 5.5$ - long-dashed curves), and fixed solar metallicity. In panels (a)–(c), $T_{\text{eff}} = 2400$ K lies at the bottom and T_{eff} decreases upward. In panel (d) the color sequence progresses from left to right as T_{eff} decreases.

For $T_{\text{eff}} \lesssim 1000$ K, the K -band flux is sensitive to gravity because it corresponds to a peak in the H_2 CIA opacity. This opacity depends quadratically on the gas number density, unlike most other opacity sources that are roughly linear functions of the density. Higher gravities cause higher photospheric pressures and a greater CIA opacity, which depresses the K -band flux. Figures 4a and 4b indeed show redder $K-L'$ and $K-[3.55]$ colors as $\log g$ increases. Only the coolest T dwarfs are affected, however, because at higher T_{eff} the H_2O opacity in the K -band increases and CIA is no longer dominant.

The effect of gravity on the IRAC colors (Figures 4c and 4d) is more subtle, and the cause varies with T_{eff} or spectral type. The chemistry of CH_4 and PH_3 , and the temperature-pressure profile, are all dependent on gravity. The net result is bluer $[4.49]-[5.73]$ colors as gravity increases, for $T_{\text{eff}} < 1400$ K, or late-L and all T types.

4.2.2. Sedimentation efficiency

Figure 5 shows that the sedimentation efficiency, which regulates the thickness of the cloud decks and the geometric depth of the photosphere, has a large effect on the near- and mid-infrared colors of ultracool dwarfs. The wavelength dependence of the cloud opacity is fairly flat in the infrared (Ackerman & Marley 2001), except for a possible silicate feature around $10 \mu\text{m}$ (Cushing et al. 2006). Hence, the cloud affects all bands from the optical to the mid-infrared. At longer wavelengths, the gas opacity tends to dominate and the mid-infrared flux is less sensitive to the choice of f_{sed} , except when the cloud is very thick ($f_{\text{sed}} \approx 1$).

The range of f_{sed} depicted in Figure 5 lies between the cloudless and thick-cloud extremes shown in Figure 4, and so the model sequences have intermediate colors. All the model color sequences in Figure 5 show a sharp reversal at $T_{\text{eff}} \approx 1300$ K. This reversal is also seen in the observed colors at the L-T transition (triangle to square symbols in the plots), where the atmospheres are changing rapidly from cloudy to cloudless. The thick-cloud model ($f_{\text{sed}} = 1$) generally gives the closest fit to all the color-color diagrams, except for $K-L'$ vs. $L'-M'$, which is better fit with cloudless models. Nonetheless, a significant mismatch remains, which compels us to explore model

parameters other than gravity and f_{sed} , in search of better agreement with the observations.

4.2.3. Metallicity

Figure 5 shows that decreasing the metallicity of the cloudless models by 0.3 dex impacts only the colors of the latest T dwarfs ($T_{\text{eff}} \lesssim 1000$ K) between 2.2 and $3.8 \mu\text{m}$. Reducing the metallicity has a qualitatively similar effect on the chemistry of C, N, and O as increasing the gravity or gas density (Lodders & Fegley 2002). The abundances of molecules composed of two metals (e.g. CO) decrease much faster than the abundances of molecules with only one metal (e.g. H_2O). Thus, CO and N_2 will be relatively less abundant than H_2O , CH_4 and NH_3 . In addition, a decrease in the metallicity reduces the H_2O abundance and the overall opacity in the atmosphere (which is dominated by H_2O absorption), and results in increased gas density. Finally, the importance of H_2 CIA increases in a metal poor atmosphere. All these effects mimic the effect of increasing gravity. The $[\text{M}/\text{H}] = -0.3$, $\log g = 5$ sequence (Figure 5) is very similar to the $[\text{M}/\text{H}] = 0$, $\log g = 5.5$ sequence (Figure 4) in all the color-color diagrams shown. In a future paper, we will explore whether decreasing metallicity or increasing gravity in dusty L dwarfs has effects similar to those of increasing sedimentation efficiency (i.e., thinning of the cloud decks), and vice versa.

4.2.4. Vertical mixing

Figures 4 and 5 show that the models with reasonable ranges of $\log g$, f_{sed} , and $[\text{M}/\text{H}]$ do not reproduce the observed colors of L and T dwarfs very well, although the general trends with T_{eff} are satisfactory. The worst mismatches are seen in the $K-L'$ and/or $L'-M'$ colors (Figures 4a and 5a), where discrepancies of up to a full magnitude are seen for the T dwarfs. The synthetic $[5.73]-[7.87]$ colors (Figures 4d and 5d) are also ~ 0.3 mag too blue. This discrepancy is consistent with the detailed fit of the SED of the T7.5 dwarf Gl 570D with the same models (Saumon et al. 2006) where the fluxes in the deep CH_4 and H_2O bands from 5.5 to $8 \mu\text{m}$ (Figure 1) are underestimated.

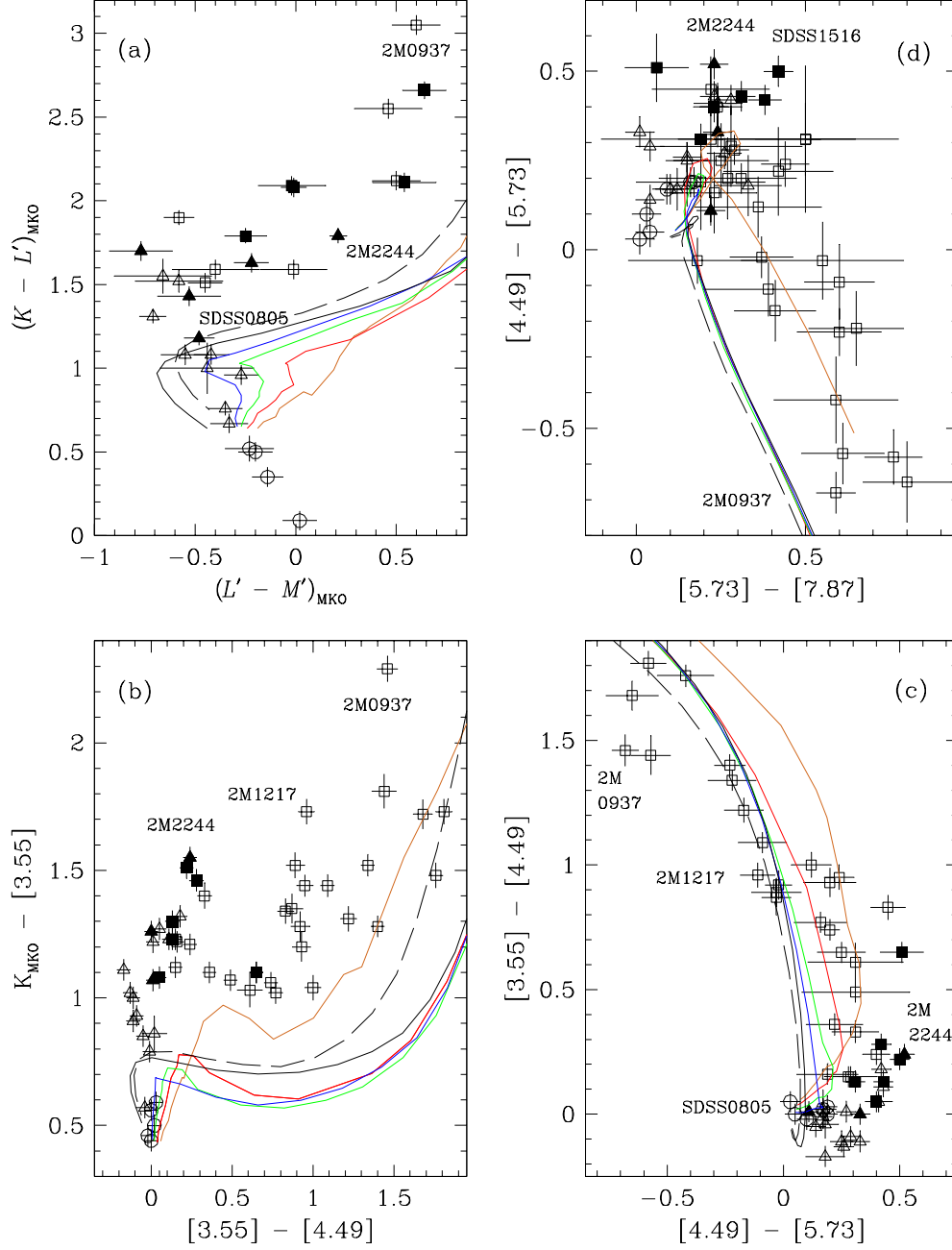


Fig. 5.— Color-color diagrams and the effect of sedimentation efficiency. The diagrams and symbols are as in Figure 4. The curves show the synthetic colors as a function of T_{eff} for five cloud models ($f_{\text{sed}} = 4$ – blue curves; $f_{\text{sed}} = 3$ – green curves; $f_{\text{sed}} = 2$ – red curves; $f_{\text{sed}} = 1$ – orange curves; cloudless – black curves), two metallicities (solar – all solid curves; $[M/H] = -0.3$ – dashed curve), and fixed $\log g = 5.0$.

It is also puzzling that the wide ranges of parameters considered so far are unable to reproduce the range in the observed colors of L dwarfs, shown as triangles in Figures 4 and 5. For example, the observed range in $K-L'$ is ~ 1 magnitude, and in $[4.49] - [5.73]$ it is ~ 0.5 magnitudes (Figure 3). The synthetic colors for the appropriate range of T_{eff} (1400 K – 2400 K, G04) only vary by ~ 0.6 magnitudes at $K-L'$ and by ~ 0.3 magnitudes at $[4.49] - [5.73]$, for $4.5 \leq \log g \leq 5.5$ and $1 \leq f_{\text{sed}} \leq 4$.

As described in §4.1, there is growing evidence that non-equilibrium chemistry caused by vertical mixing is common in T dwarfs. The spectrum of the T6 dwarf Gl 229B shows enhanced CO and depleted NH_3 (Noll et al. 1997; Oppenheimer et al. 1998; Griffith & Yelle 1999; Saumon et al. 2000), and the mid-infrared spectrum of the T7.5 dwarf Gl 570D also shows depleted NH_3 (Saumon et al. 2006). Models incorporating non-equilibrium chemistry have been shown to reproduce the M' photometry of brown dwarfs better than equilibrium models (Leggett et al. 2002; G04). Another example is shown in Figure 1: the $3\mu\text{m}$ CH_4 band in the spectrum of the L9 dwarf 2MASS J09083803+5032088 is much weaker than predicted by chemical equilibrium models with parameters appropriate for late-L field dwarfs ($T_{\text{eff}} = 1400$ K, $f_{\text{sed}} = 2$, and $\log g = 5$).

Figure 6 shows non-equilibrium models computed with two mixing efficiencies, $K_{zz} = 10^2$ and $10^4 \text{ cm}^2 \text{ s}^{-1}$. The synthetic colors are very sensitive to vertical mixing, because the filter bandpasses sample absorption features caused by molecules whose abundances are significantly affected by the mixing. Figure 1 shows that K , L' , and IRAC channels 1 and 4 sample CH_4 bands; K , M' , and IRAC channel 2 sample CO bands; and all filters (especially IRAC channels 2 and 3) are affected by H_2O bands (Saumon et al. 2003). The red part of the IRAC channel 4 flux is also affected by NH_3 absorption in the T dwarfs. Non-equilibrium effects on the CO and CH_4 bands appear below $T_{\text{eff}} \sim 1600$ K (or spectral types later than L5), at which point carbon is no longer fully sequestered in CO. All four diagrams in Figure 6 show that the 2–8 μm photometry of late-L and T dwarfs is well reproduced by models that include vertical mixing, especially when $T_{\text{eff}} \lesssim 1400$ K (or spectral types later than about

L7). Most of the data are matched by models with $K_{zz} \sim 10^4 \text{ cm}^2 \text{ s}^{-1}$, with residuals of $\lesssim 20\%$. Furthermore, the observed range in color for L and T types can be accommodated by variations in K_{zz} .

The best match to the $K-L'$ vs. $L'-M'$ diagram (Figure 6a) is obtained with the model parameters $K_{zz} = 10^4 \text{ cm}^2 \text{ s}^{-1}$, $\log g = 5$, $[\text{M}/\text{H}] = 0$, and $f_{\text{sed}} \geq 2$ (for $T_{\text{eff}} \gtrsim 1400$ K) or no clouds (for $T_{\text{eff}} \lesssim 1400$ K). The same parameters apply to the $K-[3.55]$ vs. $[3.55]-[4.49]$ diagram (Figure 6b), except that $f_{\text{sed}} = 2$ provides the best fit over the entire range of T_{eff} . Higher values of f_{sed} give equally good agreement if the gravity is increased. The models are less successful in reproducing the $[3.55]-[4.49]$ vs. $[4.49]-[5.73]$ diagram (Figure 6c). Vertical mixing has little effect in this diagram, and $f_{\text{sed}} \approx 1-2$ best matches the colors of the M and L dwarfs. Further improvement at the warm end of the color sequence can be achieved with above-solar metallicity at the expense of a worse fit at T-dwarf temperatures. Finally, the $[4.49]-[5.73]$ vs. $[5.73]-[7.87]$ diagram (Figure 6d) shows that the observed colors of the hotter objects ($[4.49]-[5.73] \gtrsim 0.1$) are best reproduced with $f_{\text{sed}} = 1$ and $K_{zz} = 10^4 \text{ cm}^2 \text{ s}^{-1}$.

To summarize, good agreement with all four color-color diagrams is obtained with models with solar metallicity, $\log g \approx 5$, $f_{\text{sed}} = 1-2$ for $T_{\text{eff}} > 1400$ K, and cloudless models at lower T_{eff} , and an eddy diffusion coefficient of $K_{zz} = 10^4 \text{ cm}^2 \text{ s}^{-1}$. The data strongly support the idea that non-equilibrium chemistry, as modelled by vertical transport, is prevalent in late-L and T dwarfs.

4.2.5. Objects with unusual colors

Several objects stand out in Figure 3 by being unusually blue or red for their spectral type in one or more colors. We use the model sequences in Figures 4–6 to make a preliminary assessment of these peculiar colors.

- The L7.5 dwarf 2MASS J22443167+2043433 is very red in $K-L'$, $L'-M'$, $K-[3.55]$, and $[4.49]-[5.73]$, suggesting that its atmosphere is very cloudy ($f_{\text{sed}} < 1$) and strongly affected by vertical mixing ($K_{zz} > 10^4 \text{ cm}^2 \text{ s}^{-1}$), as shown for example by Figure 6(b).

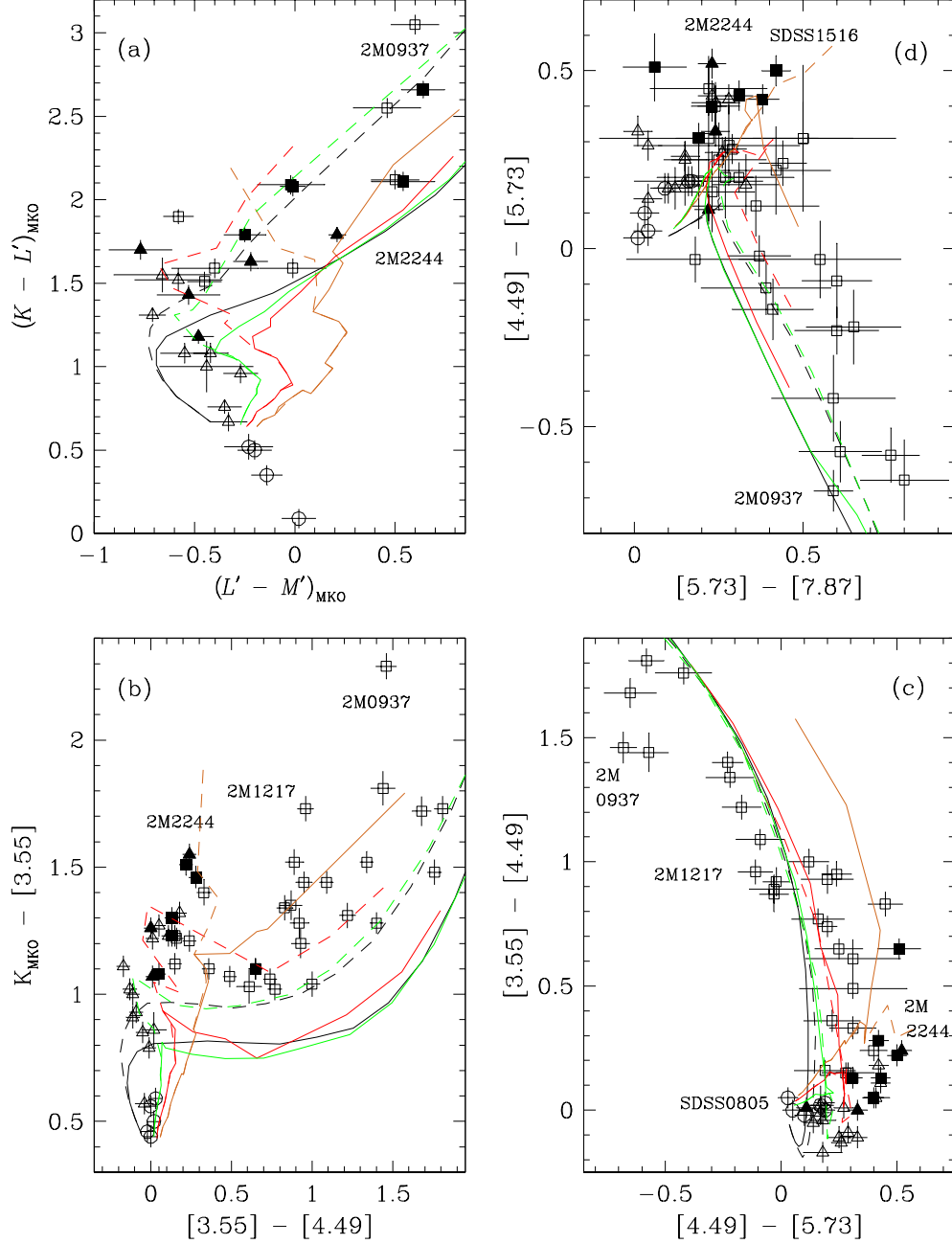


Fig. 6.— Color-color diagrams and the effect of vertical mixing. The diagrams and symbols are as in Figure 4. The curves show the synthetic colors as a function of T_{eff} for four cloud models ($f_{\text{sed}} = 3$ - green curves; $f_{\text{sed}} = 2$ - red curves; $f_{\text{sed}} = 1$ - orange curves; cloudless - black curves), two eddy diffusion coefficients ($K_{\text{zz}} = 10^2 \text{ cm}^2 \text{ s}^{-1}$ - solid curves; $K_{\text{zz}} = 10^4 \text{ cm}^2 \text{ s}^{-1}$ - dashed curves), solar metallicity, and $\log g = 5.0$.

- SDSS J133148.90-011651.4 is an L8 dwarf that is blue in $[3.55]$ – $[4.49]$ and $[4.49]$ – $[5.73]$, suggesting that it has a high value of K_{zz} and thin clouds with $f_{\text{sed}} \gtrsim 3$ (Figure 6(b)).
- SDSS J080531.80+481233 (L9.5) is blue in $[4.49]$ – $[5.73]$ and K – L' , and is similar to SDSS J133148.90-011651.4. It is best reproduced by a high sedimentation model, with $f_{\text{sed}} \sim 4$ or perhaps no clouds, and modest vertical mixing.
- The T0.5 dwarf SDSS J151643.01+305344.4 is red in K – $[3.55]$ and $[5.73]$ – $[7.87]$, which requires both vertical mixing and fairly thick clouds with $f_{\text{sed}} \leq 2$, as shown for example by Figure 6(d).
- The well-known peculiar T6 dwarf 2MASS J09373487+2931409 has such extremely red K – L' and K – $[3.55]$ colors that it can only be explained with a high gravity *and* low metallicity atmosphere, plus vertical mixing (e.g. Figures 4(b), 5(b) and 6(b)).
- 2MASS J12171110-0311131 (T7.5) is very blue in $[3.55]$ – $[4.49]$, moderately red in $[4.49]$ – $[5.73]$, and moderately blue in other colors (P06). This dwarf has a bright K -band flux peak, implying weak H_2 CIA and therefore low gravity (Burgasser et al. 2006a). However, the color sequences in Figures 4 and 5 show that decreasing gravity and increasing metallicity would not reproduce the observed colors, so the high K flux may be due to something other than low H_2 opacity. The colors may be due to extremely efficient vertical mixing, e.g., $K_{zz} \sim 10^6 \text{ cm}^2 \text{ s}^{-1}$, which leads to reduced CH_4 and brighter K and $[3.55]$ magnitudes (see Figure 6b). This T dwarf has been imaged by *HST* and appears to be single (Burgasser et al. 2006c), so duplicity does not seem to explain its unusual colors.

As we note in §4.1, the above discussion implies that all five model parameters, T_{eff} , gravity, $[\text{M}/\text{H}]$, f_{sed} and K_{zz} , can be individually varied to fit the properties of each unusual object. In fact the dynamical parameters f_{sed} and K_{zz} will depend on the other three bulk properties,

as well as on rotation and the detailed chemical composition. Further modeling of individual objects, such as 2MASS J22443167+2043433 and SDSS J133148.90-011651.4 which seemingly have similar spectral types and vertical mixing but very different f_{sed} , will help to illuminate such issues.

4.3. Effects of Gravity and Vertical Mixing on Luminosity

P06 suggest that the spread in the IRAC photometry of T dwarfs is due to variations in gravity within the sample. Except when they are very young, brown dwarfs cool at nearly constant radii and their gravity strongly correlates with their mass and their luminosity. The effect of gravity on models is therefore better revealed in color–magnitude diagrams than in color–color diagrams.

Figure 7 shows the IRAC channel 1 and 2 absolute magnitudes as functions of color, $M_{[3.55]}$ vs. $[3.55]$ – $[4.49]$ and $M_{[4.49]}$ vs. $[4.49]$ – $[5.73]$, for those objects which have measured parallaxes. The data reveal clear sequences as a function of spectral type, with increased scatter in the T dwarf regime. Evolutionary calculations indicate that for a population of very-low-mass stars and brown dwarfs older than $\gtrsim 1$ Gyr (such as our present sample), objects with lower T_{eff} will span a wider range of mass and gravity (see Figure 1 of Saumon et al. 2006). However, the model sequences shown in Figure 7 indicate that, for the plausible range of $\log g = 4.5$ – 5.5 , the width due to gravity of the modelled sequence is narrower than the observed T dwarf sequence, at least for the ($M_{[4.49]}$) vs. $[4.49]$ – $[5.73]$ diagram. We conclude that a range of gravities is not sufficient by itself to explain the width of the T dwarf sequence in these diagrams. Increasing the vertical mixing coefficient from $K_{zz} = 0$ to $10^4 \text{ cm}^2 \text{ s}^{-1}$ shifts the T dwarfs' $[3.55]$ – $[4.49]$ colors blueward and the $[4.5]$ – $[5.8]$ colors redward, by several tenths of a magnitude — and mostly recovers the observed sequence. This large shift clearly shows that a range of vertical mixing efficiency, ($K_{zz} \sim 10^2$ – $10^6 \text{ cm}^2 \text{ s}^{-1}$) in cloudless brown-dwarf atmospheres could reproduce the observed range of T dwarf 3–8 μm colors.

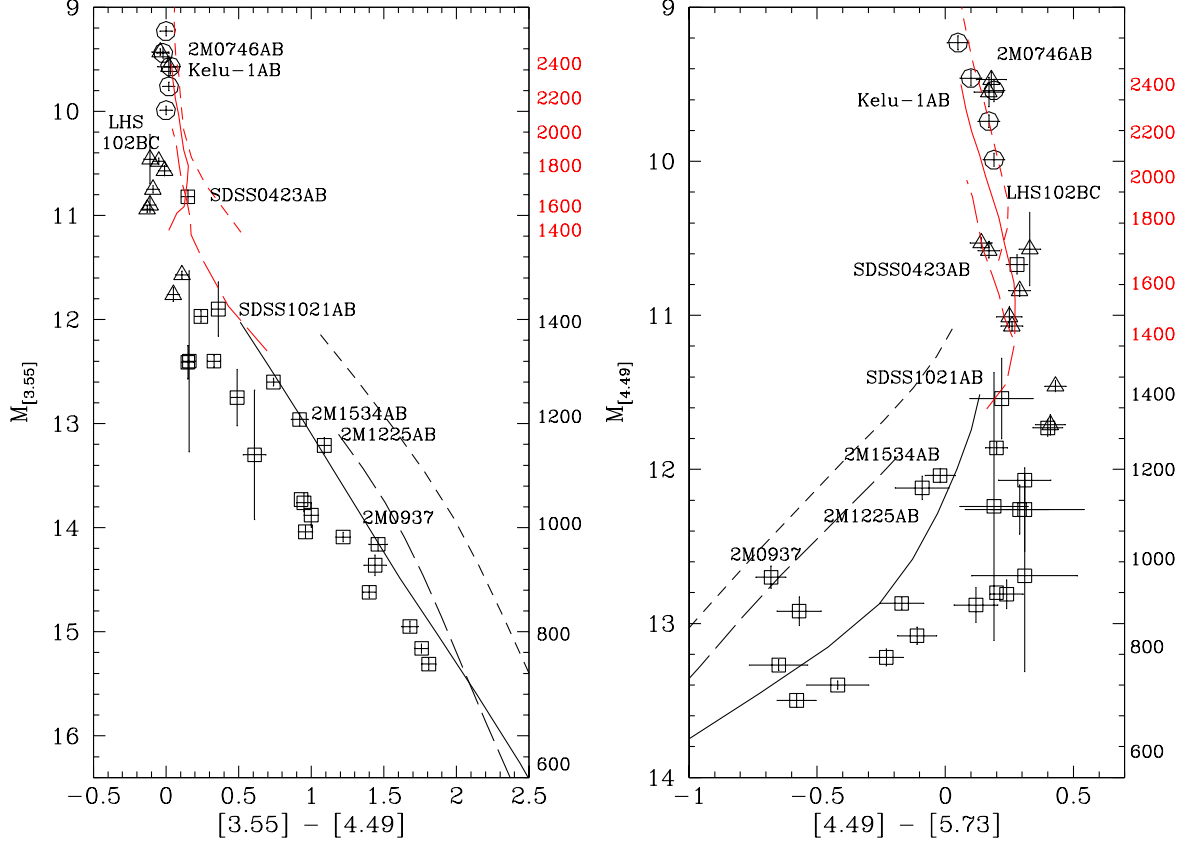


Fig. 7.— IRAC color-magnitude diagrams for those objects with measured parallax. The symbols are described in Figure 4. Known binaries (with combined photometry) are labelled, as is the peculiar T6 dwarf 2MASS J0937347+293142. Cloudy models with $f_{\text{sed}} = 2$ and $1400 \leq T_{\text{eff}} \leq 2400$ K are shown by the red curves, and cloudless models with $500 \leq T_{\text{eff}} \leq 1400$ K are shown by the black curves. The plausible range of gravity for field brown dwarfs ($\log g = 4.5\text{--}5.5$) is bracketed by the short-dashed and long-dashed curves, respectively. These sequences do not include vertical mixing. Models including vertical mixing, with $K_{zz} = 10^4 \text{ cm}^2 \text{ s}^{-1}$ and $\log g = 5$, are shown by the solid curves. Labels on the right axes indicate T_{eff} (K) for the non-equilibrium models.

5. Effective Temperature Indicators

Of the colors considered in this paper, two show promise as effective temperature indicators. Figure 3 shows that both $K-L'$ and $[3.55]-[4.49]$ exhibit relatively little scatter and vary monotonically with spectral type. The monotonicity of $K-L'$ with spectral type was first noted by Stephens et al. (2001). This relation was subsequently used by Chauvin et al. (2004) and Neuhäuser et al. (2005) to assign a spectral type and T_{eff} to candidate planetary-mass companions of more massive objects.

Figure 8 shows the observed $K-L'$ and $[3.55]-[4.49]$ colors as a function of T_{eff} , as determined by G04 and Luhman et al. (2006). Cloudy ($f_{\text{sed}}=2$) and cloudless model color sequences are also shown. The observed colors are well reproduced by the models in the appropriate range of T_{eff} when vertical mixing is included. Although $[3.55]-[4.49]$ is constant down to ~ 1700 K, the onset of CH_4 absorption moves the colors steadily redward through the late-L and the T sequences. As shown in the figure, the putative Y dwarfs (i.e., dwarfs cooler than T dwarfs) will also likely be red in both colors.

We note that care must be taken when applying empirical color- T_{eff} relations appropriate for field objects to young low-mass and low-gravity, and possibly non-solar metallicity, objects. For late-T dwarfs, H_2 CIA opacity is important, particularly in the K band, and extremely sensitive to gravity and metallicity (§4.2.1, 4.2.3). For example, for a mid-T dwarf with $K-L' \approx 2.5$, varying $\log g$ by 0.5 dex produces a change in T_{eff} of 100 K, and varying $[\text{M}/\text{H}]$ by 0.3 dex a change of ~ 50 K. In addition, $K-L'$ is sensitive to the mixing parameter K_{zz} for late-L to early-T types, and $[3.55]-[4.49]$ is also sensitive to this parameter for late-L to late-T types. Figure 8 shows that if K_{zz} is substantially larger or smaller in the atmospheres of low-mass objects, errors in derived T_{eff} of 100–300 K will result.

6. Conclusions

Our NIRI L' ($3.75 \mu\text{m}$), M' ($4.70 \mu\text{m}$), and IRAC channels 1–4 (3.55 , 4.49 , 5.73 and $7.87 \mu\text{m}$) photometry, when combined with previously published data, constitutes a sample of 30–50 objects (depending on the colors) that is large enough to

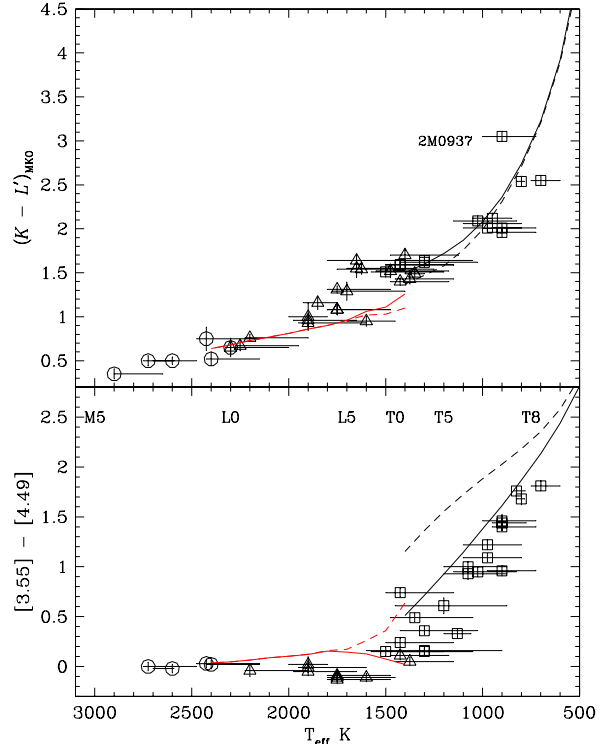


Fig. 8.— Colors as indicators of T_{eff} . The values of T_{eff} are determined from bolometric luminosities by G04 and Luhman et al. (2006); the G04 values have been revised for the binarity of Kelu-1 (Liu & Leggett 2005), LHS 102BC (Golimowski et al. 2004b), SDSS J042348.57-041403.5 (Burgasser et al. 2005) and SDSS J102109.69-030420.1 (Burgasser et al. 2006c). The symbols are described in Figure 4. Approximate spectral types are indicated, using the T_{eff} vs. spectral type relationship of G04. The errors in T_{eff} are dominated by uncertainty in age. The curves show model color sequences with $[\text{M}/\text{H}] = 0$, $\log g = 5$, and cloudless atmospheres with $500 \leq T_{\text{eff}} \leq 1400$ K (black curves) or cloudy atmospheres with $f_{\text{sed}} = 2$ and $1400 \leq T_{\text{eff}} \leq 2400$ K (red curves). The dashed curves are chemical equilibrium models ($K_{zz} = 0$) and the solid curves are non-equilibrium models with $K_{zz} = 10^4 \text{ cm}^2 \text{ s}^{-1}$. The peculiar T6 dwarf 2MASS J0937347+293142 is identified.

establish the behaviour of the entire L–T spectral sequence in color–color diagrams. Useful comparisons with synthetic mid-infrared colors are now possible. Current model atmospheres are quite complex, incorporating detailed molecular and atomic opacities, the formation and sedimentation of condensates, and vertical mixing leading to non-equilibrium chemistry.

Generally the models reproduce the observed mid-infrared colors well. For early- to mid-L dwarfs ($T_{\text{eff}} \gtrsim 1600$ K), the synthetic IRAC colors are insensitive to variations in the model parameters, except for the case of thick clouds ($f_{\text{sed}} = 1$). The colors of the late-L and T dwarfs are only reproduced by models that include non-equilibrium chemistry arising from vertical transport (mixing) in the radiative region of the atmosphere. Efficient mixing is necessary, with an eddy diffusion coefficient of $K_{zz} \approx 10^4 \text{ cm}^2 \text{ s}^{-1}$. The comparisons presented here show that vertical mixing in the atmospheres of late-L and T dwarfs ($T_{\text{eff}} \lesssim 1600$ K) affects the chemistry of carbon and is widespread among these objects.

Late-L and early-T dwarfs that are unusually red or unusually blue in the near-infrared are also red or blue, respectively, in some of the mid-infrared colors. The red objects are best reproduced by non-equilibrium models with very low sedimentation efficiency ($f_{\text{sed}} \approx 1$) and hence thick condensate cloud decks, and the blue objects are reproduced by non-equilibrium models with very high sedimentation efficiency ($f_{\text{sed}} \approx 3\text{--}4$) and hence thin condensate cloud decks.

The models account for most of the observed range in color and absolute magnitude via variations in the eddy mixing coefficient within the range $K_{zz} = 10^2\text{--}10^6 \text{ cm}^2 \text{ s}^{-1}$. The mixing mechanism in the radiative region of brown dwarf atmospheres is presently unknown, so it is not possible to assess whether such a wide range is reasonable or not. The remaining $\lesssim 20\%$ discrepancies between observed and modelled colors and magnitudes can be attributed to several possible causes, including variations in cloud properties that are not captured in our one-dimensional cloud model, uncertainties in the opacities of CH_4 and NH_3 , the choices of C, N, and O abundances, and perhaps variations in the C/O ratio in brown dwarf atmospheres.

Vertical mixing may also be an important con-

sideration for the direct detection of giant planets around nearby stars (G04; Marley et al. 2006, Hinz et al. 2006). After the discovery of Gl 229B, Marley et al. (1996) suggested that a substantial 4–5 μm flux peak should be a universal feature of giant planets and brown dwarfs. This expectation, combined with a favorable planet/star flux ratio, has made the M band a favorite for planet detection (Burrows et al. 2005, Marley et al. 2006). However, Figures 4 and 8 show that the M or 4.6 μm region is fainter – and the L or 3.6 μm region is brighter – than the equilibrium chemistry models predict, at least for $T_{\text{eff}} \gtrsim 700$ K. Given these and other considerations (such as cleaner atmospheric transmission at L compared with M) the comparative advantage of ground-based searches for young, bright giant planets at M may be somewhat less than currently expected (see also Marley et al. 2006). Another implication of the reduced M -band flux is that planetary masses (and upper limits) inferred from M -band measurements using equilibrium chemistry models (Hinz et al. 2006) will be too low.

This initial study is a comparison of observed and synthetic broadband color–color diagrams of brown dwarfs, and it is limited to identifying and interpreting trends in the data. The model parameters that best match the colors of a specific object vary with color, which, unless the models are perfect, limits the level of analysis that can be performed. Being differential in nature, colors can magnify small errors in models that otherwise agree well with the data. For example, the ~ 0.3 mag mismatch between the observed and synthetic [5.73]–[7.78] colors of late-T dwarfs (Figures 4(d), 5(d), and 6(d)) betrays the generally good fit of the same models with the entire SED of the T7.5 dwarf Gl 570D (Saumon et al. 2006). Because of the haphazard overlap of the photometric and molecular bands and the complex variations in brown dwarf spectra, color–color diagrams can be difficult to interpret. With global trends identified and generally good agreement between models and data, the detailed study of both typical and anomalous brown dwarfs can be tackled. Our analysis of ground-based and *Spitzer* photometry and spectra of such objects is underway.

We are grateful to Malcolm Currie at the Rutherford Appleton Laboratory, and the Starlink

team, for help with the NIRI data analysis. We are also grateful to Linhua Jiang of the University of Arizona for help with the IRAC data analysis. Brian Patten of CfA Harvard was very generous with pre-publication access to IRAC data and in helping with the IRAC data analysis.

This work is based in part on observations made with the *Spitzer Space Telescope*, which is operated by the Jet Propulsion Laboratory, California Institute of Technology under a contract with NASA, and on observations made at the Gemini Observatory, which is operated by the Association of Universities for Research in Astronomy Inc. (AURA), under a cooperative agreement with the NSF on behalf of the Gemini partnership: the National Science Foundation (United States), the Particle Physics and Astronomy Research Council (United Kingdom), the National Research Council (Canada), CONICYT (Chile), the Australian Research Council (Australia), CNPq (Brazil) and CONICET (Argentina).

Support for this work was provided by NASA through an award issued by JPL/Caltech. This work was also supported in part under the auspices of the U.S. Department of Energy at Los Alamos National Laboratory under Contract W-7405-ENG-36. MSM acknowledges the support of the NASA Office of Space Sciences. TRG is supported by the Gemini Observatory, which is operated by AURA on behalf of the international Gemini partnership listed above. SKL acknowledges the support of the Gemini Observatory, the Joint Astronomy Centre and the U.K. Particle Physics and Astronomy Research Council.

Funding for the SDSS and SDSS-II has been provided by the Alfred P. Sloan Foundation, the Participating Institutions, the National Science Foundation, the U.S. Department of Energy, NASA, the Japanese Monbukagakusho, the Max Planck Society, and the Higher Education Funding Council for England. The SDSS Web Site is <http://www.sdss.org/>. The SDSS is managed by the Astrophysical Research Consortium for the participating institutions: American Museum of Natural History, Astrophysical Institute Potsdam, University of Basel, Cambridge University, Case Western Reserve University, University of Chicago, Drexel University, Fermilab, Institute for Advanced Study, Japan Participation Group, Johns Hopkins University, Joint Institute

for Nuclear Astrophysics, Kavli Institute for Particle Astrophysics and Cosmology, Korean Scientist Group, Chinese Academy of Sciences (LAMOST), Los Alamos National Laboratory, Max-Planck-Institute for Astronomy (MPIA), Max-Planck-Institute for Astrophysics (MPA), New Mexico State University, Ohio State University, University of Pittsburgh, University of Portsmouth, Princeton University, United States Naval Observatory, and University of Washington.

References

- Ackerman, A. S. & Marley, M. S. 2001, *ApJ*, 556, 872
- Beichman, C. A., Chester, T. J., Skrutskie, M., Low, F. J. & Gillett, F. 1998, *PASP*, 110, 480
- Bézar, B., Lellouch, E., Strobel, D., Maillard J.-P. & Drossard, P. 2002, *Icarus*, 159, 95
- Burgasser, A. J. et al. 2002, *ApJ*, 564, 421
- Burgasser, A. J., Marley, M. S., Ackerman, A. S., Saumon, D., Lodders, K., Dahn, C. C., Harris, H. C., Kirkpatrick, J. D. 2002, *ApJ* 571, L151
- Burgasser, A. J., Reid, I. N., Leggett, S. K., Kirkpatrick, J. D., Liebert, J., Burrows, A. 2005, *ApJ*, 634, 177
- Burgasser, A. J., Burrows, A., Kirkpatrick, J. D. 2006a, *ApJ*, 639, 1095
- Burgasser, A. J., Geballe, T. R., Leggett, S. K., Kirkpatrick, J. Davy & Golimowski, D. A. 2006b, *ApJ*, 637, 1067
- Burgasser, A. J., Kirkpatrick, J. D., Cruz, K. L., Reid, I. N., Leggett, S. K., Liebert, J., Burrows, A., Brown, M. E. 2006c, *ApJ*, in press, *astro-ph/0605577*
- Burrows, A., et al. 1997, *ApJ*, 491, 856
- Burrows, A., Hubbard, W. B., Lunine, J. I., Liebert, J. 2001, *Reviews of Modern Physics*, 73, 719
- Burrows, A., Sudarsky, D., Hubeny, I. 2006, *ApJ*, 640, 1063
- Cavanagh, B., Hirst, P., Jenness, T., Economou, F., Currie, M. J., Todd, S. & Ryder, S. D., 2003, *Astronomical Data Analysis Software and Systems XII*, ASP Conference Series, Vol. 295, H. E. Payne, R. I. Jedrzejewski, and R. N. Hook,

- eds., 237
- Chauvin, G., Lagrange, A.-M., Dumas, C., Zuckerman, B., Mouillet, D., Song, I., Beuzit, J.-L., & Lowrance, P. 2004, *A&A*, 425, L29
- Chiu, K., Fan, X., Leggett, S. K., Golimowski, D. A., Zheng, W., Geballe, T. R., Schneider, D. P. & Brinkmann, J. 2006, *AJ*, 131, 2722, (C06)
- Cushing, M. C. et al. 2006, *ApJ*, 648, 614
- Dahn C. C. et al. 2002, *AJ*, 124, 1170
- Fazio, G. et al., 2004, *ApJS*, 154, 10
- Fegley, B. Jr. & Lodders, K. 1994, *Icarus*, 110, 117
- Fegley, B. Jr. & Lodders, K. 1996, *ApJ*, 472, L37
- Geballe, T. R. et al. 2002, *ApJ*, 564, 466
- Golimowski D. A. et al. 2004a, *AJ*, 127, 3516, (G04)
- Golimowski D. A. et al. 2004b, *AJ*, 128, 1733
- Griffith, C.A. & Yelle, R.V. 1999, *ApJ*, 519, L85
- Hinz, P.H., Heinze, A.N., Sivanandam, S., Miller, D.L., Kenworthy, M.A., Brusa, G., Freed, M. & Angel, J.R.P. 2006, *ApJ*, in press, astro-ph/0606129
- Hodapp, K. W. et al. 2003, *PASP*, 115, 1388
- Houck, J. et al. 2004, *ApJS*, 154, 18
- Kendall, T. R., Delfosse, X., Martín, E. L., Forveille, T. 2004, *A&A*, 416, L17
- Knapp, G. R. et al. 2004, *AJ*, 127, 3553, (K04)
- Leggett, S. K. et al. 2002, *ApJ*, 564, 452
- Leggett, S. K., Hawarden, T. G., Currie, M. J., Adamson, A. J., Carroll, T. C., Kerr, T. H., Kuhn, O. P., Seigar, M. S., Varricatt, W. P. & Wold, T. 2003, *MNRAS*, 345, 144
- Liu, M. C. & Leggett, S. K. 2005, *ApJ*, 634, 616
- Lodders, K. & Fegley, B., Jr. 2002, *Icarus*, 393, 424
- Luhman, K. L. et al. 2006, *ApJ*, in press
- Marley, M.S., Fortney, J., Seager, S., Barman, T. 2006, in *Protostars and Planets V*, B. Reipurth, Ed., in press.
- Marley, M. S., Saumon, D., Guillot, T., Freedman, R. S., Hubbard, W. B., Burrows, A., & Lunine, J. I. 1996, *Science*, 272, 1919
- Marley, M. S., Seager, S., Saumon, D., Lodders, K., Ackerman, A. S., Freedman, R. S. & Fan, X. 2002, *ApJ*, 568, 335
- Neuhäuser, R., Guenther, E. W., Wuchterl, G., Mugrauer, M., Bedalov, A., & Hauschildt, P. H. 2005, *A&A*, 435, L13
- Noll, K. S., Geballe, T. R., Leggett, S. K. & Marley, M. S. 2000, *ApJ*, 541, L75
- Noll, K.S., Geballe, T.R. & Marley, M.S. 1997, *ApJ*, 489, 87
- Noll, K.S., Knacke, R.F., Geballe, T.R. & Tokunaga, A.T. 1988, *ApJ*, 324, 1210
- Noll, K.S., & Larson, H.P. 1991, *Icarus*, 89, 168
- Patten, B. M., et al. 2006, *ApJ*, in press, astro-ph/0606432
- Reid, I. N. & Cruz, K. L. 2002, *AJ*, 123, 466
- Roellig, T. L., et al. 2004, *ApJS*, 154, 418
- Saumon, D., Geballe, T. R., Leggett, S. K., Marley, M.S., Freedman, R. S., Lodders, K., Fegley, B., Jr. & Sengupta, S. K. 2000, *ApJ*, 541, 374
- Saumon, D., Marley, M.S., Cushing, M.C., Leggett, S.K., Roellig, T.L., Lodders, K. & Freedman, R.S. 2006, *ApJ*, in press, astro-ph/0605563
- Saumon, D., Marley, M. S., Lodders, K. & Freedman, R. S. 2003, *Brown Dwarfs*, Proceedings of IAU Symposium 211, ed. E. Martín. San Francisco: Astronomical Society of the Pacific, 2003, 345
- Simons, D. A. & Tokunaga, A. 2002, *PASP*, 114, 169
- Skrutskie, M. F. et al. 2006, *AJ*, 131, 1163
- Stephens, D. C., Marley, M. S., Noll, K. S., & Chanover, N. 2001, *ApJ*, 556, L97
- Tokunaga, A. T., Simons, D. A. & Vacca, W. D. 2002, *PASP*, 114, 180
- Toon, O.B., McKay, C.P., Ackerman, T.P. & Sathanam, K. 1989, *JGR* 94, 16287
- Vrba, F. J. et al. 2004, *AJ*, 127, 2948
- Werner, M., et al. 2004, *ApJS*, 154, 1
- York, D. G. et al. 2000, *AJ*, 120, 1579

TABLE 1
GEMINI NIRI L' AND M' PHOTOMETRY (MKO SYSTEM)

Name	Type ¹	L' (error) (mag)	Date (YYMMDD)	M' (error) (mag)	Date (YYMMDD)	Notes
SDSS J000013.54+255418.6	T4.5	13.03(0.03)	040826	13.28(0.10)	040801	...
2MASS J00345157+0523050	T6.5	13.30(0.04)	040827	12.66(0.10)	040827	...
2MASS J02431371-2453298	T6	13.27(0.16)	050128	...
SDSS J080531.80+481233	L9.5	12.34(0.04)	041230	12.81(0.07)	041230,050115	2,3
SDSS J083008.12+482847.4	L9	12.75(0.15)	040405	...
SDSS J085758.45+570851.4	L8	11.55(0.10)	040405	4,5
SDSS J111010.01+011613.1	T5.5	13.89(0.05)	050115	4
SDSS J133148.90-011651.4	L8	12.73(0.03)	050115	2
2MASS J15031961+2525196	T5	11.92(0.04)	040509	6
2MASS J15530228+1532369AB	T7	13.83(0.05)	050115	13.29(0.15)	040406	7
2MASS J16322911+1904407	L7.5	13.07(0.15)	040530	...
2MASS J22443167+2043433	L7.5	11.90(0.03)	040801	4

¹ Spectral types are based on near-infrared classification schemes for L dwarfs (Geballe et al. 2002) and T dwarfs (Burgasser et al. 2006b).

² Near-infrared colors are unusually blue for this spectral type.

³ G04 reported $L' = 12.31 \pm 0.05$.

⁴ Near-infrared colors are unusually red for this spectral type.

⁵ Leggett et al. (2002) reported $M' = 11.50 \pm 0.05$.

⁶ G04 reported $M' = 12.25 \pm 0.15$.

⁷ T7 type applies to unresolved pair. Burgasser et al. (2006c) report T6.5+T7.

TABLE 2
FILTER BANDPASSES AT OPERATIONAL TEMPERATURES

Filter Name	Nominal Wavelength (μm)	50% Cut- On (μm)	50% Cut- Off (μm)
L'_{MKO}	3.75	3.43	4.11
M'_{MKO}	4.70	4.57	4.80
IRAC channel 1	3.55	3.18	3.92
IRAC channel 2	4.49	4.00	5.01
IRAC channel 3	5.73	5.02	6.43
IRAC channel 4	7.87	6.45	9.33

TABLE 3
Spitzer IRAC PHOTOMETRY

Name	Type ¹	Channel 1			Channel 2			Channel 3			Channel 4			Date (YYMMDD)	Notes
		mJy	[3.55]	% err	mJy	[4.49]	% err	mJy	[5.73]	% err	mJy	[7.87]	% err		
SDSS J000013.54+255418.6	T4.5	0.91	13.72	1.0	1.06	13.07	2.0	1.09	12.56	10.0	0.64	12.50	1.0	050725	2
SDSS J075840.33+324723.4	T2	3.05	12.41	0.4	2.52	12.13	0.5	2.37	11.71	1.8	1.89	11.33	4.0	051023	...
SDSS J080531.80+481233	L9.5	2.98	12.44	0.5	1.92	12.43	0.5	1.36	12.32	1.1	0.93	12.10	1.8	051022	3
SDSS J105213.51+442255.7	T0.5	1.43	13.23	0.1	1.03	13.10	0.2	0.98	12.67	0.5	0.73	12.36	0.8	051127	...
SDSS J115553.86+055957.5	L7.5	2.07	12.83	0.2	1.33	12.83	0.3	1.15	12.50	1.0	0.80	12.26	2.0	051229	...
SDSS J120747.17+024424.8	T0	2.01	12.86	0.2	1.46	12.73	0.3	1.24	12.42	1.5	0.82	12.23	5.0	060706	...
SDSS J151643.01+305344.4	T0.5	1.01	13.61	0.5	0.79	13.39	1.0	0.80	12.89	1.0	0.66	12.47	2.0	050724	4
SDSS J152039.82+354619.8	T0	1.87	12.94	0.5	1.25	12.89	0.2	1.16	12.49	1.2	0.80	12.26	0.8	050726	...
2MASS J22443167+2043433	L7.5	3.22	12.35	0.4	2.58	12.11	0.5	2.65	11.59	0.9	1.83	11.36	1.5	050723	5

¹ Spectral types are based on near-infrared classification schemes for L dwarfs (Geballe et al. 2002) and T dwarfs (Burgasser et al. 2006b).

² Nearby bright star caused more uncertain photometry. Sky values were interpolated between the diffraction spikes of the bright star.

³ Near-infrared colors are unusually blue for this spectral type.

⁴ Near-infrared colors are unusually red for this spectral type.

⁵ Near-infrared colors are extremely red for this spectral type.